

Global Distribution of Fe K α Lines in the Galactic Center Region Observed with the Suzaku Satellite

Hideki UCHIYAMA

Department of Physics, Graduate School of Science, The University of Tokyo, 7-3-1 Hongo, Bunkyo-ku, Tokyo 113-0033
uchiyoama@junio.phys.s.u-tokyo.ac.jp

Masayoshi NOBUKAWA, Takeshi GO TSURU, Katsuji KOYAMA

Department of Physics, Graduate school of Science, Kyoto University, Oiwake-cho, Kitashirakawa, Kyoto 606-8502
and

Hironori MATSUMOTO

Kobayashi-Maskawa Institute for the Origin of Particles and the Universe, Nagoya University, Furo-cho, Chikusa-ku, Nagoya, 464-8602

(Received ; accepted)

Abstract

We have surveyed spatial profiles of the Fe K α lines in the Galactic center diffuse X-rays (GCDX), including the transient region from the GCDX to the Galactic ridge X-ray emission (GRXE), with the Suzaku satellite. We resolved Fe K α line complex into three lines of FeI, FeXXV and FeXXVI K α , and obtained their spatial intensity profiles with the resolution of $\sim 0.1^\circ$. We compared the FeXXV K α profile with a stellar mass distribution (SMD) model made from near infrared observations. The intensity profile of FeXXV K α is nicely fitted with the SMD model in the GRXE region, while that in the GCDX region shows 3.8 ± 0.3 ($0.2^\circ < |l| < 1.5^\circ$) or 19 ± 6 ($|l| < 0.2^\circ$) times excess over the best-fit SMD model in the GRXE region. Thus FeXXV K α in the GCDX is hardly explained by the same origin of the GRXE. In the case of point source origin, a new population with the extremely strong FeXXV K α line is required. An alternative possibility is that the majority of the GCDX is truly diffuse optically thin thermal plasma.

Key words: Galaxy: Center—Inter stellar medium— X-ray spectra

1. Introduction

Diffuse X-rays were discovered from the inner disk of the Milky Way Galaxy with the HEAO-1 satellite (Worrall et al. 1982), and called as the Galactic ridge X-ray emission (GRXE). EXOSAT observed more details and found that the GRXE were extended by about $\pm 60^\circ$ in longitude and $\pm (1^\circ - 2^\circ)$ in latitude (Warwick et al. 1985). The Tenma satellite discovered strong emission lines at the energy of about 6.7 keV (here the 6.7-keV line) in the GRXE (Koyama et al. 1986). The Ginga satellite made survey observations along the Galactic plane with the 6.7-keV line, and found a flux peak at the Galactic center with the width of about 1° . We call this peak as the Galactic center diffuse X-rays (GCDX) (Koyama et al. 1989; Yamauchi et al. 1990; Yamauchi & Koyama 1993).

The ASCA satellite separated the 6.7-keV line in the GCDX into three emission lines at 6.4, 6.7 and 7.0 keV, which were respectively identified as K α lines from neutral (FeI), He-like (FeXXV) and H-like (FeXXVI) iron (Koyama et al. 1996). For the GRXE, the Suzaku satellite resolved the Fe K α lines (Ebisawa et al. 2008). The strongest emission line in the GCDX and GRXE is FeXXV K α at 6.7 keV, and hence would be due to an optically thin thermal plasma. From the flux ratio of FeXXVI K α /FeXXV K α , the plasma temperature of the GCDX was estimated to be around $kT = 5 - 10$ keV (e.g. Koyama et al. 2007b; Yamauchi et al. 2009).

Since spectra of the GCDX and GRXE have spatial temperature variations and/or may be contaminated by possible non-thermal emissions, we concentrate on the flux of FeXXV K α line as a pure component of the thin thermal plasma. Previous studies of the Fe K α lines with the Ginga and RXTE satellites (Yamauchi & Koyama 1993; Revnivtsev et al. 2006) had limited spatial resolutions (FWHM $\sim 1^\circ - 2^\circ$) compared to the size of the GCDX, and the FeXXV K α line flux was contaminated by the adjacent FeI and XXVI K α lines due to the limited energy resolutions (FWHM ~ 1.1 keV at 6 keV). Yamauchi et al. (2009) reported that the intensity ratio of the three Fe K α lines has spatial dependence and hence to resolve the three lines is essential for the study the nature of FeXXV K α line. This paper reports, for the first time, the FeXXV K α line distributions in the GCDX and the transient region from the GCDX to the GRXE ($-3^\circ < l < 2^\circ$, $-2^\circ < b < 1^\circ$) with the CCD cameras on-board the Suzaku satellite.

The observations and data reduction are described in section 2. The analysis and the intensities of FeI K α , FeXXV K α and FeXXVI K α are given in section 3. In section 4, we compare the FeXXV K α profiles of the GCDX and GRXE with that of a stellar mass model made from near infrared (NIR) observations. Based on the profile comparison between NIR stars and FeXXV K α , we discuss origin of the GCDX. In this paper, uncertainties are quoted at the 90% confidence range unless otherwise

stated.

2. Observations and Data Reduction

The data in this paper were obtained from September 2005 to March 2009 with the X-ray Imaging Spectrometer (XIS) onboard the Suzaku satellite. Most of the data were observed as the Suzaku Key project observation. The total effective exposure is about 3.2 Ms. The details of these observations are summarized in table 1.

The XIS contains four sets of X-ray CCD camera systems (XIS 0, 1, 2, and 3) placed on the focal planes of four X-Ray Telescopes (XRTs) onboard the Suzaku satellite. XIS 0, 2, and 3 have front-illuminated (FI) CCDs, while XIS 1 has a back-illuminated (BI) CCD. Detailed descriptions of the Suzaku satellite, the XRT, and the XIS can be found in Mitsuda et al. (2007), Serlemitsos et al. (2007), and Koyama et al. (2007a), respectively.

In these observations, the XIS was operated in the normal clocking full window mode, with the time resolution of 8.0 s. One of the FI CCD cameras (XIS 2) has been out of function since November 2006, and hence 71% of the total exposure was observed without XIS 2. Although the XIS CCDs were significantly degraded by on-orbit particle radiation, the CCD performance had been calibrated well with the checker-flag charge-injection (CI) method (Nakajima et al. 2008; Ozawa et al. 2009) until October 2006, and has been restored with the spaced-row CI (SCI) method (Prigozhin et al. 2008; Uchiyama et al. 2009). The SCI method was used in 75% of the total exposure. The XIS 2 and SCI status in the observations is shown in table 1.

We reprocessed the data using the calibration data base (CALDB) released at 2008-10-20 and `xispi` in the HEADAS software package version 6.6.1. We confirmed that the center energy of Mn I $K\alpha$ line of the onboard calibration sources (^{55}Fe) was consistent with 5.895 eV within the calibration uncertainty of 20 eV, and the energy resolutions were 130–180 eV (FWHM) at 5.9 keV during the observations.

3. Analysis and Results

In order to investigate intensity profiles of Fe $K\alpha$ lines along the Galactic longitude and latitude, X-ray spectra were made from the rectangles shown in figures 1a and b, respectively. The sizes of the rectangles along the longitude (figure 1a) are $6' \times 12'$ (0.1° in longitude and 0.2° in latitude), while those along the latitude (figure 1b) are $12' \times 6'$ (0.2° in longitude and 0.1° in latitude). Here we adopted a new coordinate as $(l_*, b_*) = (l + 0.056, b + 0.046)$, where the origin of this coordinate $(l_*, b_*) = (0^\circ, 0^\circ)$ is the position of Sgr A* (Reid & Brunthaler 2004) and the $b_* = 0^\circ$ line corresponds the Galactic plane. With this new coordinate, the centers of each rectangle along the longitude (figure 1a) are given as $(l_*, b_*) = (0.1^\circ \times n, 0^\circ)$ where n is an integer number. The centers of each rectangle along the latitude (figure 1b) are $b_* = 0.1^\circ \times n$ and $l_* = -1.104, -0.784, -0.504, -0.114, 0.226, 0.556,$

0.876 and 1.226 . To extend the profile to larger b_* values, we used the data at $(l_*, b_*) = (0.056, -1.954)$ (OBSID 502059010). Since the Fe $K\alpha$ flux at this position is lower than any other regions, we made a spectrum of $17' \times 17'$ rectangle. To make spectra of diffuse emission, bright sources listed in table 2 and the CCD corners illuminated by the calibration sources were excluded from all the rectangles.

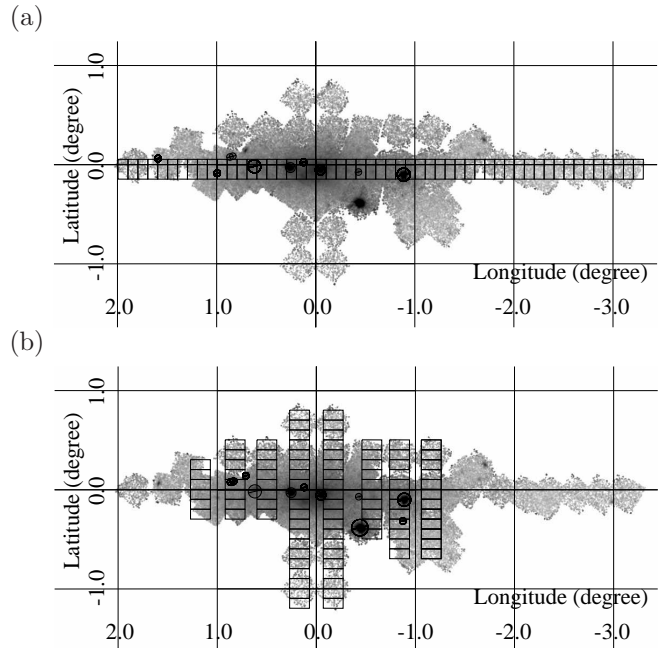


Fig. 1. (a) The rectangles to extract X-ray spectra for the longitudinal distribution overlaid on the Suzaku XIS image in the 6.55–6.8 keV band. Bright point source regions (circles, see table 2) are excluded before making the spectra. (b) Same as (a) but for the latitudinal distribution.

Using `xissimarfgn` (Ishisaki et al. 2007) and `xismfngn`, the effective area of the XRT and the response of the XIS were calculated, and ancillary response files and redistribution matrix files were made for each observation. Since the responses of the FIs are almost the same, we merged the FI spectra.

The non X-ray background (NXB) spectra sorted by the cut-off rigidity were made from the same source region in the detector coordinate using `xisnxbgen` (Tawa et al. 2008). The spectra of NXB were subtracted from those of the GCDX.

We fitted the spectra in the 5–10 keV band with a phenomenological model which consists of four Gaussians and an absorbed power-law continuum. The line centers of the Gaussians were fixed to 6.40 (Fe I $K\alpha$), 6.68 (Fe XXV $K\alpha$), 6.97 (Fe XXVI $K\alpha$) and 7.06 (Fe I $K\beta$) keV according to the APEC model (Smith et al. 2001) and Kaastra & Mewe (1993). The intrinsic widths of these lines were fixed to 0 eV. The intensities of the Fe I $K\alpha$, Fe XXV $K\alpha$, and Fe XXVI $K\alpha$ lines in the model were free parameters. The intensity of the Fe I $K\beta$ line was fixed to 0.125 times that of the Fe I $K\alpha$ line according to Kaastra & Mewe (1993).

Table 1. Observation data list.

OBSID	Pointing direction				Observation		Exp. (ks)	XIS 2*	SCI†	Object name
	$\alpha_{2000.0} (^{\circ})$	$\delta_{2000.0} (^{\circ})$	$l (^{\circ})$	$b (^{\circ})$	Start (UT)	End (UT)				
100027010	266.51	-28.92	0.05	-0.07	2005-09-23T10:17:18:25	2005-09-24T11:05:19	44.7	ok	off	Sgr A East
100027020	266.30	-29.17	-0.25	-0.05	2005-09-24T14:17:17	2005-09-25T17:27:19	37.4	ok	off	Sgr A west
100037010	266.30	-29.17	-0.25	-0.05	2005-09-29T04:35:41	2005-09-30T04:29:19	43.5	ok	off	Sgr A west
100037030	266.20	-29.35	-0.45	-0.07	2005-09-30T06:06:32	2005-09-30T07:41:20	3.0	ok	off	KS1741-293(GCBGD2)
100037040	266.51	-28.93	0.06	-0.07	2005-09-30T07:43:01	2005-10-01T06:21:24	42.9	ok	off	Sgr A East
100037060	266.88	-28.44	0.64	-0.10	2005-10-10T12:28:01	2005-10-12T07:05:23	76.4	ok	off	Sgr B2
500018010	266.16	-29.47	-0.57	-0.09	2006-02-20T12:45:25	2006-02-23T10:50:14	106.9	ok	off	SGR C
500005010	266.77	-28.63	0.43	-0.12	2006-03-27T23:00:22	2006-03-29T18:12:15	88.4	ok	off	GC CENTER #2
100048010	266.51	-28.93	0.06	-0.07	2006-09-08T02:23:24	2006-09-09T09:06:15	63.0	ok	off	GALACTIC CENTER
501040010	266.69	-28.38	0.61	0.07	2006-09-21T17:29:01	2006-09-23T06:52:20	61.4	ok	on	GC SGR B NORTH
501040020	266.69	-28.38	0.61	0.07	2006-09-24T05:03:12	2006-09-25T07:00:24	44.8	ok	on	GC SGR B NORTH
501008010	266.50	-29.17	-0.15	-0.19	2006-09-26T14:18:16	2006-09-29T21:25:14	129.6	ok	on	GC SOUTH
501009010	266.19	-28.91	-0.07	0.18	2006-09-29T21:26:07	2006-10-01T06:55:19	51.2	ok	on	GC SOUTH BGD
501010010	266.26	-30.37	-1.29	-0.64	2006-10-07T02:16:52	2006-10-08T10:19:19	50.7	ok	off	HESS J1745-303
501049010	265.38	-29.75	-1.17	0.33	2006-10-08T10:22:40	2006-10-09T02:19:24	19.6	ok	on	GALACTIC CENTER
501050010	265.91	-29.65	-0.83	0.00	2006-10-09T02:20:25	2006-10-09T13:39:24	22.0	ok	on	GALACTIC CENTER
501051010	265.70	-29.93	-1.17	-0.00	2006-10-09T13:40:09	2006-10-10T06:44:24	21.9	ok	on	GALACTIC CENTER
501052010	265.50	-30.21	-1.50	0.00	2006-10-10T06:45:09	2006-10-10T21:18:14	19.3	ok	on	GALACTIC CENTER
501053010	265.30	-30.50	-1.83	-0.00	2006-10-10T21:18:59	2006-10-11T10:06:14	21.9	ok	on	GALACTIC CENTER
501057010	266.03	-30.11	-1.17	-0.33	2006-10-11T10:07:27	2006-10-12T03:28:14	20.5	ok	on	GALACTIC CENTER
501039010	267.02	-28.35	0.78	-0.16	2007-03-03T12:20:20	2007-03-05T12:39:25	96.4	on	on	GC SGR B EAST
501046010	265.98	-28.90	-0.17	0.33	2007-03-10T15:03:10	2007-03-11T03:55:14	25.2	on	on	GALACTIC CENTER
501047010	265.78	-29.19	-0.50	0.33	2007-03-11T03:55:59	2007-03-11T19:04:14	25.6	on	on	GALACTIC CENTER GC2
501048010	265.58	-29.47	-0.83	0.33	2007-03-11T19:04:59	2007-03-12T08:09:14	27.5	on	on	GALACTIC CENTER GC3
501054010	266.63	-29.25	-0.17	-0.33	2007-03-12T08:11:07	2007-03-12T23:58:24	26.1	on	on	GALACTIC CENTER GC9
501055010	266.43	-29.54	-0.50	-0.33	2007-03-12T23:59:09	2007-03-13T15:40:19	27.2	on	on	GALACTIC CENTER GC10
501056010	266.23	-29.82	-0.83	-0.33	2007-03-13T15:41:12	2007-03-14T05:00:24	26.5	on	on	GALACTIC CENTER GC11
501058010	266.98	-27.72	1.30	0.20	2007-03-14T05:02:29	2007-03-15T18:55:14	63.3	on	on	GC SGR D NORTH
501059010	267.09	-27.94	1.17	0.00	2007-03-15T18:55:51	2007-03-17T05:06:19	62.2	on	on	GC SGR D
501060010	267.29	-27.65	1.50	0.00	2007-03-17T05:07:04	2007-03-18T20:58:14	64.8	on	on	GC SGR D EAST
502022010	266.81	-28.88	0.23	-0.27	2007-08-31T12:33:33	2007-09-03T19:00:25	134.8	on	on	(L,B)=(0.25,-0.27)
102013010	266.51	-28.93	0.06	-0.07	2007-09-03T19:01:10	2007-09-05T05:20:20	51.4	on	on	GALACTIC CENTER
502020010	267.19	-28.13	1.05	-0.17	2007-09-06T00:26:47	2007-09-09T16:10:19	139.1	on	on	SGR D SNR
502002010	267.16	-29.14	0.17	-0.67	2007-10-09T16:40:54	2007-10-10T03:40:24	23.2	on	on	GC14
502003010	266.96	-29.42	-0.17	-0.67	2007-10-10T03:41:13	2007-10-10T15:20:24	21.5	on	on	GC15
502004010	267.48	-29.31	0.17	-1.00	2007-10-10T15:21:17	2007-10-11T01:00:24	19.9	on	on	GC16
502005010	267.29	-29.60	-0.17	-1.00	2007-10-11T01:01:17	2007-10-11T11:32:20	20.6	on	on	GC17
502006010	266.18	-28.62	0.17	0.33	2007-10-11T11:34:01	2007-10-11T23:07:14	22.6	on	on	GC18
502007010	265.86	-28.45	0.17	0.67	2007-10-11T23:09:15	2007-10-12T09:52:14	22.0	on	on	GC19
502008010	265.66	-28.73	-0.17	0.67	2007-10-12T09:52:59	2007-10-12T21:50:19	23.8	on	on	GC20
502009010	267.48	-27.37	1.83	-0.00	2007-10-12T21:52:24	2007-10-13T07:30:19	20.9	on	on	GC21
502010010	266.38	-28.34	0.50	0.33	2007-10-13T07:32:00	2007-10-13T18:50:24	21.6	on	on	GC22
502011010	266.57	-28.05	0.83	0.33	2007-10-13T18:51:09	2007-10-14T05:30:24	23.0	on	on	GC23
502016010	266.23	-30.11	-1.08	-0.48	2008-03-02T18:08:00	2008-03-04T17:40:19	70.5	on	on	HESS J1745-303 1
502017010	266.47	-30.09	-0.95	-0.65	2008-03-06T13:26:36	2008-03-08T16:00:24	72.6	on	on	HESS J1745-303 2
502018010	266.06	-30.24	-1.27	-0.43	2008-03-08T16:02:17	2008-03-10T21:00:19	79.0	on	on	HESS J1745-303 3
502051010	266.94	-28.15	0.91	0.01	2008-03-11T06:19:45	2008-03-15T05:30:18	138.8	on	on	GC G0.9+0.1
502059010	268.38	-29.96	-0.00	-2.00	2007-09-29T01:40:51	2007-10-02T14:10:16	136.8	on	on	GALACTIC BULGE
503007010	266.44	-28.57	0.33	0.17	2008-09-02T10:15:27	2008-09-03T22:52:24	52.2	on	on	GC LARGEPROJECT1
503008010	266.78	-29.13	0.00	-0.38	2008-09-03T22:53:29	2008-09-05T06:56:19	53.7	on	on	GC LARGEPROJECT2
503009010	266.45	-29.34	-0.33	-0.24	2008-09-05T06:57:08	2008-09-06T15:55:24	52.4	on	on	GC LARGEPROJECT3
503010010	266.04	-29.55	-0.70	-0.05	2008-09-06T15:56:13	2008-09-08T01:39:24	53.1	on	on	GC LARGEPROJECT4
503011010	265.95	-29.83	-0.97	-0.13	2008-09-08T09:08:09	2008-09-09T21:33:19	57.6	on	on	GC LARGEPROJECT5
503012010	266.30	-29.94	-0.91	-0.44	2008-09-14T19:35:07	2008-09-16T00:50:14	57.7	on	on	GC LARGEPROJECT6
503013010	265.67	-30.07	-1.30	-0.05	2008-09-16T00:51:19	2008-09-18T04:44:24	104.8	on	on	GC LARGEPROJECT7
503014010	265.18	-30.75	-2.10	-0.05	2008-09-18T04:46:49	2008-09-19T07:32:20	55.4	on	on	GC LARGEPROJECT8
503015010	265.03	-30.96	-2.35	-0.05	2008-09-19T07:33:05	2008-09-20T09:56:13	56.8	on	on	GC LARGEPROJECT9
503016010	264.87	-31.17	-2.60	-0.05	2008-09-22T06:47:49	2008-09-23T08:07:17	52.2	on	on	GC LARGEPROJECT10
503017010	264.72	-31.38	-2.85	-0.05	2008-09-23T08:08:10	2008-09-24T09:21:13	51.3	on	on	GC LARGEPROJECT11
503018010	264.56	-31.60	-3.10	-0.05	2008-09-24T09:27:54	2008-09-24T22:30:24	29.4	on	on	GC LARGEPROJECT12
503072010	265.99	-29.21	-0.42	0.17	2009-03-06T02:39:11	2009-03-09T02:55:24	140.6	on	on	EXTENDED CHIMNEY
403009010	266.48	-28.78	0.17	0.02	2009-03-21T02:03:27	2009-03-23T18:26:09	110.8	on	on	ARCHES CLUSTER

*The XIS2 column shows whether the XIS 2 worked ("ok") or not in the observation.

†The SCI column shows whether the SCI mode was on or off in the observation.

The normalization, photon index, and interstellar absorption of the absorbed power-law model were free. The cross section of the photoelectric absorption was obtained from Morrison & McCammon (1983).

The FIs and BI spectra were fitted simultaneously. We did not use the BI data above 8 keV, because the NXB fluxes become high in this energy band. If one rectangle region overlaps more than two separate observations, we made separate spectra and were fitted simultaneously.

Some examples of the spectra and the best-fit models are shown in figure 2. In these figures, we find some residuals at 8–9 keV band, which are identified as Fe XXV K β , Ni XXVII K α and other weak lines (Koyama et al. 2007b). Inclusion of these lines, however, does not change the best-fit intensities of the Fe K α lines. The best-fit intensities of the three iron lines and the 5–10 keV band are shown in table 3. The profiles of the Fe XXV K α line intensity along

the Galactic longitude ($b_* = 0^\circ$) and latitude ($l_* = -0^\circ 11'$) are shown in figure 3 as examples.

We see global symmetry between the intensities in the positive and negative l_* (figure 3a) and b_* (figure 3b), except for the region of $|l_*| = 0^\circ 1 - 0^\circ 3$ in figure 3a (see section 4.3).

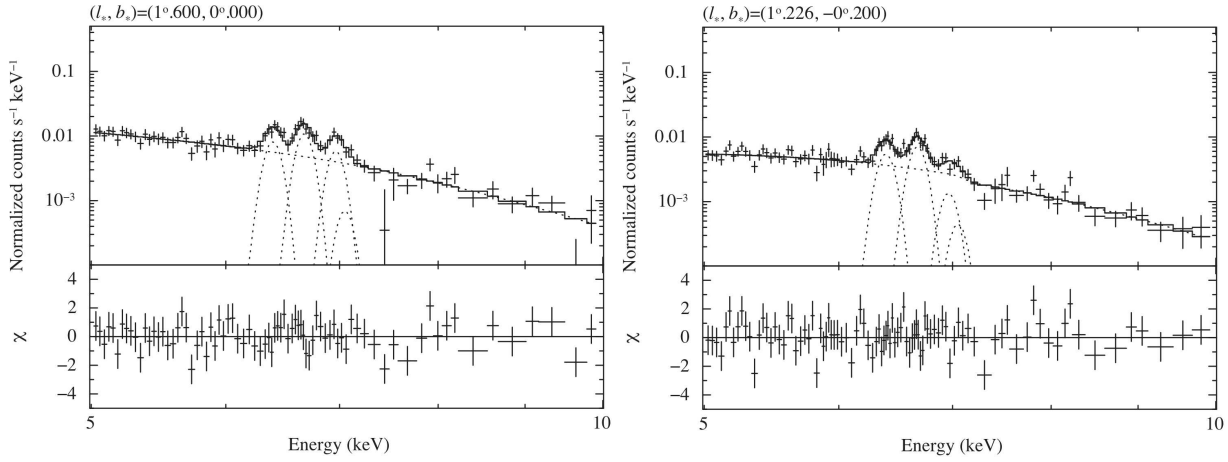
4. Discussion

4.1. The distributions of the Fe XXV K α line and the stellar mass

Using the intensity profile, origin of the Fe XXV K α line in the GCDX is discussed in comparison with that in the GRXE. We fitted the profile of the Fe XXV K α line with a stellar mass distribution (SMD) model which was originally compiled by Munro et al. (2006), based on the NIR observations (Launhardt et al. 2002; Kent et al. 1991).

Table 2. The positions and radii of bright X-ray sources excluded before making the diffuse X-ray spectra.

Name	Position		Radius
	l	b	
1E 1740.7–2942	$-0^{\circ}887$	$-0^{\circ}097$	$4'$
CXOGCS J174445.5–295042	$-0^{\circ}774$	$-0^{\circ}062$	$2'$
2E 1742.9–2929	$-0^{\circ}439$	$-0^{\circ}383$	$5'$
KS 1741–293	$-0^{\circ}432$	$-0^{\circ}074$	$3'$
Sgr A East	$-0^{\circ}047$	$-0^{\circ}053$	$3'$
Arches cluster	$0^{\circ}123$	$0^{\circ}024$	$2'$
1E 1743.1–2843	$0^{\circ}256$	$-0^{\circ}029$	$3'$
G0.61+0.01	$0^{\circ}620$	$0^{\circ}016$	$4'$
CXOGC J174645.3–281546	$0^{\circ}712$	$0^{\circ}141$	$2'$
HD 161507	$0^{\circ}837$	$0^{\circ}085$	$2'$
G0.9+0.1	$0^{\circ}866$	$0^{\circ}077$	$2'$
SAX J1748.2–2808	$0^{\circ}994$	$-0^{\circ}086$	$2'$
AX J1749.1–2733	$1^{\circ}592$	$-0^{\circ}062$	$2'$

**Fig. 2.** Left panel: an example of the spectra for the longitudinal distribution with the best-fit model (solid line). Dotted Gaussians are $K\alpha$ lines of Fe I, Fe XXV and Fe XXVI. The weak line in the right is Fe I $K\beta$. For simplicity, only the FIs spectra are shown. The vertical bars show the 1σ errors. Residuals from the best-fit model near at 8–9 keV are due to Ni XXVII $K\alpha$ and Fe XXV $K\beta$ and other weak lines (see text). Right panel: the same as the left panel, but that for the latitudinal distribution data.**Table 3.** List of observed intensities.*

Galactic coordinate				Observed intensity [†]							Flag [‡]
l (°)	b (°)	l_* (°)	b_* (°)	Fe I K α		Fe XXV K α		Fe XXVI K α		5–10 keV	
-0.156	-0.046	-0.100	0.000	7.31	(6.83–7.72)	18.4	(17.7–18.9)	7.97	(7.44–8.42)	20.7	l
-0.056	-0.046	0.000	0.000	12.4	(11.5–13.3)	45.5	(44.3–46.7)	13.4	(12.9–14.3)	44.3	l
0.044	-0.046	0.100	0.000	35.2	(34.8–35.7)	24.3	(23.9–24.7)	9.49	(9.14–9.85)	39.0	l
0.500	-0.146	0.556	-0.100	8.35	(8.05–8.65)	8.05	(7.75–8.36)	3.14	(2.88–3.41)	11.3	b
0.500	-0.046	0.556	0.000	9.95	(9.71–10.3)	10.2	(9.95–10.5)	3.25	(3.01–3.52)	13.7	b
0.500	0.054	0.556	0.100	4.79	(4.51–5.02)	9.06	(8.68–9.32)	2.28	(2.02–2.53)	9.83	b
0.000	-2.000	0.056	-1.954	0.04	(0.00–0.12)	0.64	(0.55–0.74)	0.27	(0.18–0.36)	1.08	o

*This table is available in its entirety as a machine-readable form in the online journal (see the PASJ web site). A portion is shown here for guidance regarding its form and contents.

[†]The interstellar absorption is not corrected. The units are 10^{-7} photons $s^{-1} cm^{-2} arcmin^{-2}$ and 10^{-14} erg $s^{-1} cm^{-2} arcmin^{-2}$, for the Fe $K\alpha$ lines and the 5–10 keV band, respectively. Parentheses show the 90% error ranges.

[‡]The flags l , b and o mean that the data are obtained along the Galactic longitude (figure 1a), the latitude (figure 1b) and from $(l_*, b_*) = (0^{\circ}056, -1^{\circ}954)$, respectively.

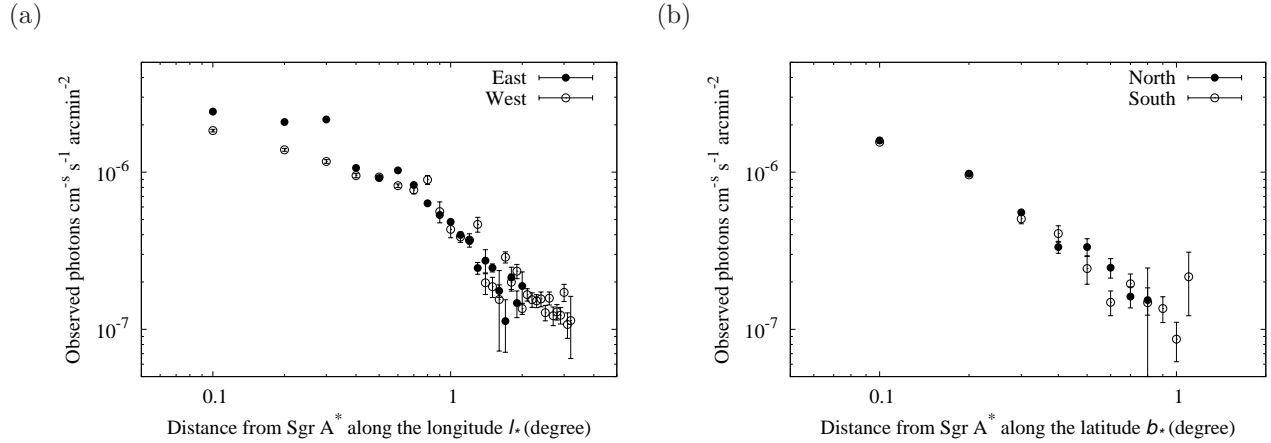


Fig. 3. (a) Observed intensity profiles of the Fe XXV K α along the Galactic longitude ($b_* = 0^\circ$). The bars show the 1σ errors. (b) The same as (a) but for the latitude distribution at $l_* = -0.114$.

The SMD model consists of four components of the nuclear stellar cluster (NSC), the nuclear stellar disk (NSD), the Galactic bulge (GB) and the Galactic disk (GD). The details of the SMD model are described in Appendix.

We made simultaneous fit for the longitudinal distribution (figure 1a) and for many latitudinal distributions (figure 1b). In this fitting, we included the results of Koyama et al. (2007b) ($|l_*| < 0.4^\circ$), Yamauchi et al. (2009) ($|l_*| > 8^\circ$) and the result of $(l_*, b_*) = (0.056, -1.954)$. These data were added in the longitudinal plot in figures 4a and c, except for those of Yamauchi et al. (2009) of $|b| > 0.15$. The additional data points in figures 4a and c are not exactly on $b_* = 0^\circ$. However, in the simultaneous fitting, the real coordinate values were taken into account.

4.1.1. The GRXE region

The intensity distribution of the Fe K α line along the Galactic plane has been already reported by Yamauchi & Koyama (1993) and Revnivtsev et al. (2006). Since Revnivtsev et al. (2006) found that the Fe K α line intensity profile agrees well with the NIR profile in the GRXE region using the RXTE data, we first tried to fit the data of $|l_*| > 1.5$ regions and $|b_*| > 0.5$ regions simultaneously with the SMD model. We assumed that the mass emissivities (see equation A7) for each component are the same, i.e. $\varepsilon_{\text{NSC}} = \varepsilon_{\text{NSD}} = \varepsilon_{\text{GD}} = \varepsilon_{\text{GB}} = \varepsilon$. Thus the free parameter was only one, ε or the normalization. The best-fit parameter was $\varepsilon = (5.85 \pm 0.03) \times 10^{33} \text{ photons s}^{-1} M_\odot^{-1}$. The fitting result for the longitudinal distribution is given in figure 4a, while that of the latitude at $l_* = -0.114$ is given in figure 4b as a typical example.

As is shown in figure 4a, we obtained a nice fit in the GRXE data of $|l_*| > 1.5$, in which the GD and partly GB components mainly contribute in the SMD model. Figure 4b also shows reasonable fit in the region of $|b_*| > 0.6$, where the GD and GB components contribute equally.

We checked the consistency between the Suzaku results (figure 4) and those of Revnivtsev et al. (2006) (figure 3 in their paper). The data in the GRXE region of $|l_*| = 10^\circ - 20^\circ$ were compared since the limited spatial resolution of RXTE made it impossible to resolve the detailed structure

around the Galactic center (GCDX). The result of figure 4a is purely for Fe XXV K α line and the Fe XXV K α line intensity at $|l_*| = 10^\circ - 20^\circ$ is about $1 \times 10^{-7} \text{ photons cm}^{-2} \text{ s}^{-1} \text{ arcmin}^{-2}$, while that of Revnivtsev et al. (2006) is the sum of Fe I, XXV and XXVI K α lines of about $4.5 \times 10^{-4} \text{ photons cm}^{-2} \text{ s}^{-1} \text{ deg}^{-2}$ (hence $1.3 \times 10^{-7} \text{ photons cm}^{-2} \text{ s}^{-1} \text{ arcmin}^{-2}$). The Fe K α line complex in the RXTE data was not separated into the three lines because of the limited energy resolution. From table 1 of Ebisawa et al. (2008) and also from figure 3 of Yamauchi et al. (2009), we estimated the mean flux ratio of Fe I, XXV and XXVI K α lines as 0.2 : 1.0 : 0.2. Thus the Fe XXV K α flux is about 70% of the total flux of Fe K α line complex. Taking this flux ratio into account, our results are consistent with that of Revnivtsev et al. (2006). We, therefore, do not discuss origin of Fe XXV K α line in the GRXE further than Revnivtsev et al. (2006).

4.1.2. The combined regions of the GCDX and GRXE

In the previous section 4.1.1, we found that Fe XXV K α profile in the GCDX shows clear excess above the SMD model which gave a nice fit to that in the GRXE. As is shown in figure 4a, this excess in the GCDX is confined in the region of the NSC and NSD. Therefore we fitted the whole data of Fe XXV K α line (the GCDX+GRXE region) simultaneously, fixing $\varepsilon_{\text{GD}} = \varepsilon_{\text{GB}} = 5.85 \times 10^{33} \text{ photons s}^{-1} M_\odot^{-1}$ and two free parameters of ε_{NSC} and ε_{NSD} . The best-fit results are given in figures 4c and d, which show globally a good fit with the enhanced parameter values of ε_{NSC} and ε_{NSD} . The best-fit ε_{NSC} and ε_{NSD} are listed in table 4. As is found from table 4, we needed 3.8 ± 0.3 and 19 ± 6 times higher emissivities in the NSC and NSD region (GCDX) than that in the GD+GB region (GRXE).

The fitting in which the mass emissivities of the NSD and NSC (ε_{NSD} and ε_{NSC}) are fixed to the same value of the GD and GB, but the stellar masses of the NSC and NSD (ρ_c and ρ_d) are free parameters (see equation A1 and A2) gives that respective stellar masses of the NSC and the NSD are 3.8 ± 0.3 and 19 ± 6 times larger than those obtained with the NIR observations (Launhardt et al. 2002), normalized to the Galactic ridge.

In section 4.3, we will discuss the origin of Fe XXV $K\alpha$ line in the GCDX based on these results.

4.2. Systematic error for Fe XXV $K\alpha$ line profile and the SMD model

Since the statistics is limited, present spectral analysis in the small region (0.1×0.2) cannot confine the interstellar absorption (N_H) within reasonable errors. We therefore did not correct the absorption effect for the flux of Fe XXV $K\alpha$. The largest interstellar absorption is $N_H \sim 6 \times 10^{22} \text{ cm}^{-2}$ near the Galactic center (Predehl 1995). Using the cross section of the photoelectric absorption of Morrison & McCammon (1983), we estimated that the flux of Fe XXV $K\alpha$ is reduced only by 9% in the largest case of $N_H = 6 \times 10^{22} \text{ cm}^{-2}$. Since the largest reduction is expected in the GCDX region, the excess discussed in section 4.1.2 becomes even larger by about 10%, if we correct the interstellar absorption. A larger error is in the making of the SMD model, which is estimated to be about 50% (Muno et al. 2006) (see Appendix). Taking these errors into account, our conclusion of the large excess of Fe XXV $K\alpha$ line at the GCDX to the GRXE in the best-fit SMD model is still valid, and hence no essential change of the discussion is required.

4.3. Origin of Fe XXV $K\alpha$ line in the GCDX

We found that the mass emissivity of Fe XXV $K\alpha$ line in the GCDX region (NSC and NSD) shows excess of 3.8 ± 0.3 (NSC) and 19 ± 6 (NSD) times larger than that in the GRXE region (GD and GB), or the stellar masses in the NSC and NSD regions are 3.8 ± 0.3 and 19 ± 6 times larger than those estimated with the NIR observations. Integrating over the whole region of the NSC and NSD, we obtain that the total stellar mass in the NSC and NSD are about $1.4 \times 10^9 M_\odot$ for the former case, which is fully consistent with the kinematic mass distribution (see figure 14 of Launhardt et al. 2002). However the latter case requires total stellar mass within the NSC and NSD to be $5.3 \times 10^9 M_\odot$, which is unacceptably large. We hence ignore the latter possibility, and discuss based on the former possibility.

Origin of Fe XXV $K\alpha$ line in the GCDX therefore cannot be the same as that in the GRXE. Yamauchi et al. (2009) found that the line intensity ratio of Fe XXVI $K\alpha$ to Fe XXV $K\alpha$ in $|l_*| < 0.3$ is higher than that in $|l_*| > 8^\circ$, which also supports that origin of Fe XXV $K\alpha$ line in the GCDX may be different from that in the GRXE. Revnivtsev et al. (2009) resolved more than 80% of the Fe $K\alpha$ flux at $(l, b) = (0.1, -1.4)$ into point sources. Although this fact supports that origin of Fe XXV $K\alpha$ line in the GRXE is due to point sources, that in the GCDX is not yet answered. As is shown by the arrows in figures 4b and 4d, Fe XXV $K\alpha$ from this region is due to the sum of nearly equal contribution of the GD and GB (the GRXE components) and not the GCDX components (the NSC and NSD).

If we assume that origin of Fe XXV $K\alpha$ line in the GCDX is an ensemble of point sources with the same populations in the GRXE region, the iron abundances in the GCDX

should be $3.8(\pm 0.3)$ – $19(\pm 6)$ times larger than that in the GRXE. This is unlikely because the abundance of iron has been reported at most two times of solar in the GCDX region (e.g. Koyama et al. 2007b; Nobukawa et al. 2010).

Another possibility is that the point source population in the GCDX is different from that in the GRXE. We see the Fe XXV $K\alpha$ intensity excess in the positive l_* side (east) compared to the negative side (west) at $|l_*| = 0.1$ – 0.3 (see figure 3a). This excess is globally associated to the clusters of high mass stars such as the Arches and Quintuplet clusters. Muno et al. (2009) also reported that the number density of X-ray stars in these regions exceeds that in the surroundings. They proposed that the excess is due to massive stars associated to the high activity of star formation in this region. The most probable massive stars are WR or OB stars. These stars often show moderately large equivalent width of Fe XXV $K\alpha$ ($EW_{6.7}$) similar to the GCDX (e.g. Skinner et al. 2007; Hyodo et al. 2008). These massive stars might contribute to not only the Arches and Quintuplet clusters but also the entire GCDX. These stars are relatively bright with the typical X-ray luminosity of $\sim 10^{34} \text{ erg s}^{-1}$ (Portegies Zwart et al. 2002; Wang et al. 2006). The deep Chandra observation revealed that point sources with the luminosity larger than $10^{32} \text{ erg s}^{-1}$ contribute less than 10% of the GCDX (see figure 6 of Revnivtsev et al. 2007). We therefore concluded that massive stars do not mainly contribute to Fe XXV $K\alpha$ line in the GCDX.

On the other hand, it may be conceivable that faint X-ray point sources with the flux below the current detection limits largely contribute to the GCDX. The most probable candidate sources for the Fe XXV $K\alpha$ line are cataclysmic variables (CVs), because their spectra are represented by high temperature plasma with large $EW_{6.7}$ and are associated with the 6.4 and 7.0 keV lines, very similar to those of the GCDX in the Fe $K\alpha$ line band. The mean $EW_{6.7}$ for X-ray bright CVs in the luminosity range of $10^{30-33} \text{ erg s}^{-1}$ is about 200 eV (Ezuka & Ishida 1999; Rana et al. 2006), while those of the GCDX and GRXE are 450–550 eV (Yamauchi et al. 2009). Thus even for the GRXE, the faint (unresolved X-ray) CVs should have, at least, two times larger $EW_{6.7}$ than the bright CVs. In addition, the number density of such (X-ray) faint CVs relative to near infrared stars should be $3.8(\pm 0.3)$ – $19(\pm 6)$ times larger than that in the GRXE to explain the observed Fe XXV line excess in the GCDX. This possibility does not violate the total mass constraint of the NSC and NSD ($\sim 1.4 \times 10^9 M_\odot$), because the mass contribution of CVs to that of the SMD (mass of infrared stars) is only a small fraction (see e.g., Pretorius et al. 2007 and references there in). For relatively bright CVs, however, such number density excess in the GCDX region has not been reported (Revnivtsev et al. 2008). For faint CVs, studies for the spatial profile have not been done well. In order to settle these potential problems in the point source origin, deep observations, with lower detection limit than the current value by orders of more than 1–2 are required.

An alternative possibility is that the majority of the GCDX (NSC and NSD) comes from diffuse optically thin

Table 4. Best-fit result with the stellar mass distribution model.

Component	Mass emissivity of the Fe XXV K α line ε *
Nuclear stellar cluster	111 ± 37
Nuclear stellar disk	22 ± 2
Galactic disk [†]	5.85 (fixed)

* See equation A7. The units are 10^{33} photons $\text{s}^{-1} M_{\odot}^{-1}$.

[†] Mass emissivities of the Galactic bulge and the Galactic disk are fixed to the best-fit of $|l_*| > 1.5^\circ$ and $|b_*| > 0.5^\circ$ regions.

thermal plasma as already proposed by Koyama et al. (2007b). Although the total flux of the Fe XXV K α line in the NSC and NSD regions is hardly explained by point sources, the spatial distributions are similar to the shapes of the NSC and NSD. The diffuse plasma, therefore, should be closely related to the ensemble of point sources. One possibility is that the plasma is made by multiple supernova explosions. This may be conceivable because the NSC and NSD regions are distinguished from the other regions (GB and GD) in respect to supernova activities; i.e., very high density of molecular gas and on-going star formation.

5. Summary

1. We have obtained intensity profiles of the Fe I, Fe XXV, and Fe XXVI K α lines in the Galactic center region of $-3^\circ < l < 2^\circ$ and $-2^\circ < b < 1^\circ$.
2. The intensity profile of Fe XXV K α is nicely fitted with the SMD model in the GRXE region ($|l_*| > 1.5^\circ$ or $|b_*| > 0.6^\circ$), while that in the GCDX ($|l_*| < 1.5^\circ$ and $|b_*| < 0.6^\circ$) shows $3.8(\pm 0.3)$ – $19(\pm 6)$ times excess over the best-fit SMD model to the profile of the GRXE region.

Appendix. Stellar Mass Distribution Model of the Milky Way Galaxy

This appendix describes the details of the three-dimensional stellar mass distribution (SMD) and actual two-dimensional fitting model (SMD model) in section 4. The SMD model was originally compiled by Munro et al. (2006) using the results of Launhardt et al. (2002) and Kent et al. (1991) based on near infrared (NIR) observations with COBE, IRAS and IRT (Boggess et al. 1992; Clegg 1980; Koch et al. 1982). The major emission sources at the NIR wavelength (1–7 μm) are main-sequence stars and thus the NIR emission is a good tracer of the stellar mass. The stellar mass model consists of the components of the nuclear stellar cluster (NSC), the nuclear stellar disk (NSD), Galactic bulge (GB) and Galactic disk (GD). In order to describe the three-dimensional stellar mass distribution of these components, we defined the X-Y-Z coordinate, where Sgr A* is located at the origin (x, y, z) = (0, 0, 0), and the Galactic plane is the X-Y plane.

The sun is assumed to be at (8500, 0, 16) in units of pc.

The stellar mass density model ρ_* ($M_{\odot} \text{ pc}^{-3}$) is $\rho_* = \rho_{\text{NSC}} + \rho_{\text{NSD}} + \rho_{\text{GD}} + \rho_{\text{GB}}$. The details of each component are described below.

The NSC component is

$$\rho_{\text{NSC}} = \frac{\rho_c}{1 + (r/r_c)^{n_c}}, \quad (\text{A1})$$

where $r = (x^2 + y^2 + z^2)^{1/2}$ is the distance from the coordinate origin (0, 0, 0), Sgr A*. The parameters are $r_c = 0.22$ pc, $\rho_c = 3.3 \times 10^6 M_{\odot} \text{ pc}^{-3}$ ($r < 6$ pc), $9.0 \times 10^7 M_{\odot} \text{ pc}^{-3}$ ($6 \leq r < 200$ pc) and $n_c = 2$ ($r < 6$ pc), 3 ($6 \leq r < 200$ pc).

The NSD and GD components are respectively given as,

$$\rho_{\text{NSD}} = \rho_d \left(\frac{r}{r_d} \right)^{-n_d} \exp \left(-\frac{|z|}{z_d} \right), \quad (\text{A2})$$

and

$$\rho_{\text{GD}} = \rho_{\text{gd}} \exp \left(-\frac{r}{r_{\text{gd}}} \right) \exp \left(-\frac{|z|}{z_{\text{gd}}} \right), \quad (\text{A3})$$

where $r = (x^2 + y^2)^{1/2}$ and z are the distance from Sgr A* in the Galactic plane and the height from the Galactic plane, respectively. The parameters for the NSD are $r_d = 1$ pc, $z_d = 45$ pc, and $n_d = 0.1$ ($r < 120$ pc), 3.5 ($120 \leq r < 220$ pc), 10 ($220 \leq r < 2000$ pc). We took $\rho_d = 300 M_{\odot} \text{ pc}^{-3}$ for $r < 120$ pc, and adjusted ρ_d to make the function continuous at $r = 120$ and 220 pc. The parameters for the GD are $\rho_{\text{gd}} = 5 M_{\odot} \text{ pc}^{-3}$, $r_{\text{gd}} = 2700$ pc and $z_{\text{gd}} = 200$ pc.

The GB component is modeled as a triaxial “generalized ellipsoidal” bar (Athanasoulas et al. 1990; Freudenreich 1998). Since the major axis of this “ellipsoid” is tilted from any of the X-, Y- and Z-axis, we defined a new coordinate X'-Y'-Z' by rotating the X-Y-Z coordinate along the Z-axis by 15° to the east and along the Y-axis by 1° to the north. In the new coordinate X'-Y'-Z', the GB is given by;

$$\rho_{\text{GB}} = \rho_{\text{gb}} \exp(-r_s), \quad (\text{A4})$$

$$r_s = \left[r_{\perp}^{c_{\parallel}} + \left(\frac{|z'|}{a_z} \right)^{c_{\parallel}} \right]^{1/c_{\parallel}}, \quad (\text{A5})$$

$$r_{\perp} = \left[\left(\frac{|x'|}{a_x} \right)^{c_{\perp}} + \left(\frac{|y'|}{a_y} \right)^{c_{\perp}} \right]^{1/c_{\perp}}. \quad (\text{A6})$$

The parameters are $\rho_{\text{gb}} = 8 M_{\odot} \text{ pc}^{-3}$, $a_x = 1100$ pc, $a_y = 360$ pc, $a_z = 220$ pc, $c_{\parallel} = 3.2$ and $c_{\perp} = 1.6$.

For the three-dimensional mass distribution function $\rho(x, y, z)$ of the components NSC (A1), NSD (A2), GD (A3) and GB (A4–6), we defined the mass emissivity of Fe XXV K α line ε (in units of photons $\text{s}^{-1} M_{\odot}^{-1}$) to be the ratio of Fe XXV K α photons emitted from a unit stellar (infrared stars) mass per second. The number of Fe XXV K α photons emitted per second from a small volume in the solid angle Ω (a rectangle of $0.1^\circ \times 0.2^\circ$) and depth Δs at the distance s from the Sun toward (l_* , b_*) direction is given as $\Omega s^2 \Delta s \varepsilon \rho$. The observed flux $\Delta F(l_*, b_*)$ from

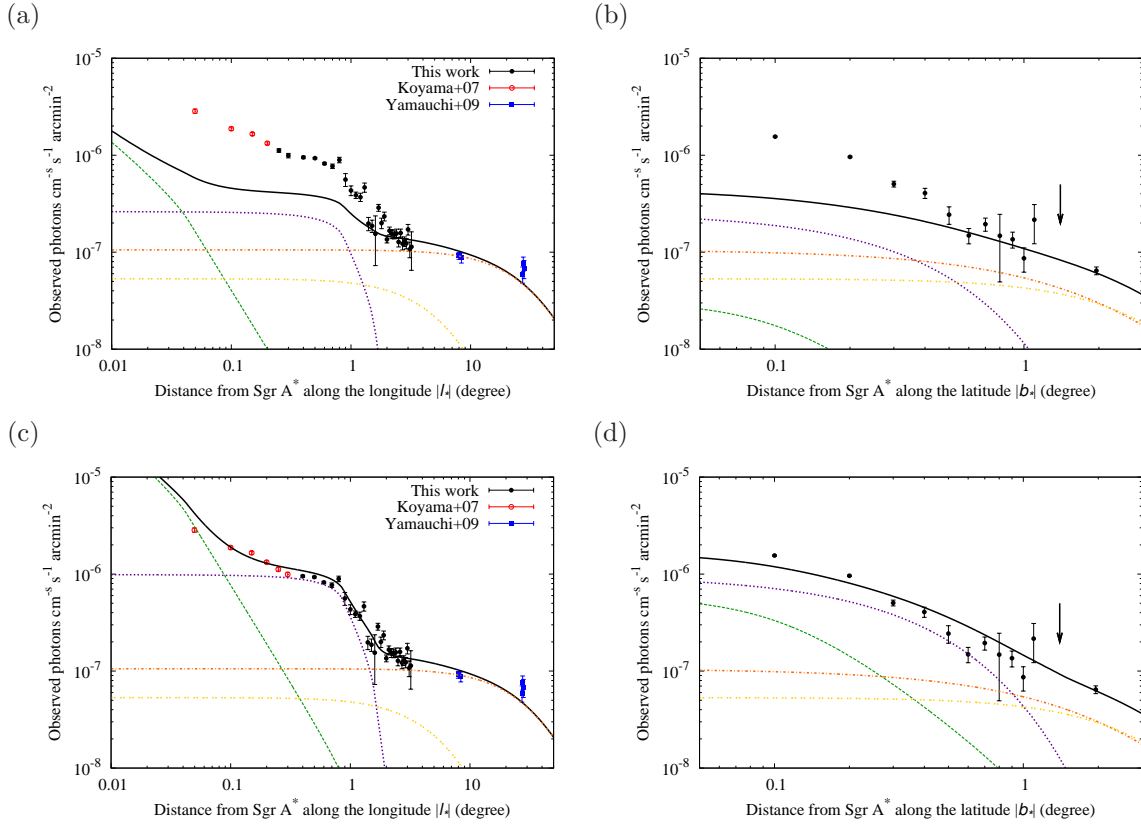


Fig. 4. (a) The FeXXV K α line intensity distribution along the Galactic plane as a function of l_* (distance from Sgr A*). For simplicity, only negative l_* region is shown, except for those at $|l_*| > 8^\circ 0$ because the model in these region (Galactic disk) is symmetric with respect to the positive and negative l_* . The green, purple, orange and yellow lines are the best-fit SMD model of the nuclear stellar cluster (NSC), nuclear stellar disk (NSD), Galactic disk (GD) and Galactic bulge (GB), respectively. The black solid line is the sum of the four components of NSC, NSD, GD and GB. The emissivities of these components are fixed to be the same. The data of $|l_*| > 1^\circ 5$ and $|b_*| > 0^\circ 5$ regions are used simultaneously in the fitting. (b) The same as the left panel (a), but those along the Galactic longitude at $l_* = -0^\circ 114$ as a function of b_* (distance from the Galactic plane). The arrow shows the position of $b = -1^\circ 4$ which is almost the same region as Revnivtsev et al. (2009). For simplicity, only negative b_* region is shown. (c) The same as the upper panel (a) but with the best-fit model in the whole region (GRXE and GCDX) with free parameters of the emissivities (or stellar mass densities) of NSC and NSD. (d) The same as the upper panel (b) but with the best-fit model same as the panel (c).

the small volume should be $\Omega s^2 \Delta s \varepsilon \rho / 4\pi s^2 = \Omega \varepsilon \rho \Delta s / 4\pi$. Then the observed flux of Fe XXV K α is given by the line-of-sight integration along s ,

$$F(l_*, b_*) = \frac{\Omega}{4\pi} \int_0^\infty (\varepsilon_{\text{NSC}} \rho_{\text{NSC}} + \varepsilon_{\text{NSD}} \rho_{\text{NSD}} + \varepsilon_{\text{GD}} \rho_{\text{GD}} + \varepsilon_{\text{GB}} \rho_{\text{GB}}) ds. \quad (\text{A7})$$

This equation is used for the fitting of observed intensity profile of Fe XXV K α line (figure 4 in the text). The overall uncertainty in building of this model is estimated to be about 50% (Muno et al. 2006).

The authors thank all of the Suzaku team members, especially M. Sawada, T. Yuasa, and K. Makishima for their comments and useful information. This work is supported by the Grant-in-Aid for the Global COE Program “The Next Generation of Physics, Spun from Universality and Emergence” and Challenging Exploratory Research

(KK) from the Ministry of Education, Culture, Sports, Science and Technology (MEXT) of Japan. HU is supported by Japan Society for the Promotion of Science (JSPS) Research Fellowship for Young Scientists. HM is supported by Grant-in-Aid for Scientific Research (B) (22340046) from JSPS.

References

- Athanassoula, E., Morin, S., Wozniak, H., Puy, D., Pierce, M. J., Lombard, J., & Bosma, A. 1990, MNRAS, 245, 130
- Boggess, N. W., et al. 1992, ApJ, 397, 420
- Clegg, P. E. 1980, Phys. Scr., 21, 678
- Ebisawa, K., et al. 2008, PASJ, 60, 223
- Ezuka, H. & Ishida, M. 1999, ApJS, 120, 277
- Freudenreich, H. T. 1998, ApJ, 492, 495
- Hyodo, Y., Tsujimoto, M., Koyama, K., Nishiyama, S., Nagata, T., Sakon, I., Murakami, H., & Matsumoto, H. 2008, PASJ, 60, 173

- Ishisaki, Y., et al. 2007, PASJ, 59, 113
- Kaastra, J. S., & Mewe, R. 1993, A&AS, 97, 443
- Kent, S. M., Dame, T. M., & Fazio, G. 1991, ApJ, 378, 131
- Koch, D., et al. 1982, Optical Engineering, 21, 141
- Koyama, K., Makishima, K., Tanaka, Y., & Tsunemi, H. 1986, PASJ, 38, 121
- Koyama, K., Awaki, H., Kunieda, H., Takano, S., & Tawara, Y. 1989, Nature, 339, 603
- Koyama, K., Maeda, Y., Sonobe, T., Takeshima, T., Tanaka, Y., & Yamauchi, S. 1996, PASJ, 48, 249
- Koyama, K., et al. 2007a, PASJ, 59, 23
- Koyama, K., et al. 2007b, PASJ, 59, 245
- Launhardt, R., Zylka, R., & Mezger, P. G. 2002, A&A, 384, 112
- Mitsuda, K., et al. 2007, PASJ, 59, 1
- Morrison, R. & McCammon, D. 1983, ApJ, 270, 119
- Muno, M. P., Bauer, F. E., Bandyopadhyay, R. M., & Wang, Q. D. 2006, ApJS, 165, 173
- Muno, M. P., et al. 2009, ApJS, 181, 110
- Nakajima, H., et al. 2008, PASJ, 60, 1
- Nobukawa, M., Koyama, K., Tsuru, T. G., Ryu, S. G., & Tatischeff, V. 2010, PASJ, 62, 423
- Ozawa, M., et al. 2009, PASJ, 61, 1
- Portegies Zwart, S. F., Pooley, D., & Lewin, W. H. G. 2002, ApJ, 574, 762
- Predehl, P. 1995, Advances in Space Research, 16, 159
- Pretorius, M. L., Knigge, C., O'Donoghue, D., Henry, J. P., Gioia, I. M., & Mullis, C. R. 2007, MNRAS, 382, 1279
- Prigozhin, G., Burke, B., Bautz, M., Kissel, S., & Lamarr, B. 2008, IEEE Transactions on Electron Devices, 55, 2111
- Rana, V. R., Singh, K. P., Schlegel, E. M., & Barrett, P. E. 2006, ApJ, 642, 1042
- Reid, M. J., & Brunthaler, A. 2004, ApJ, 616, 872
- Revnivtsev, M., Molkov, S., & Sazonov, S. 2006, MNRAS, 373, L11
- Revnivtsev, M., Vikhlinin, A., & Sazonov, S. 2007, A&A, 473, 857
- Revnivtsev, M., Sazonov, S., Krivonos, R., Ritter, H., & Sunyaev, R. 2008, A&A, 489, 1121
- Revnivtsev, M., Sazonov, S., Churazov, E., Forman, W., Vikhlinin, A., & Sunyaev, R. 2009, Nature, 458, 1142
- Serlemitsos, P. J., et al. 2007, PASJ, 59, 9
- Skinner, S. L., Zhekov, S. A., Güdel, M., & Schmutz, W. 2007, MNRAS, 378, 1491
- Smith, R. K., Brickhouse, N. S., Liedahl, D. A., & Raymond, J. C. 2001, ApJL, 556, L91
- Tawa, N., et al. 2008, PASJ, 60, 11
- Uchiyama, H., et al. 2009, PASJ, 61, 9
- Wang, Q. D., Dong, H., & Lang, C. 2006, MNRAS, 371, 38
- Worrall, D. M., Marshall, F. E., Boldt, E. A., & Swank, J. H. 1982, ApJ, 255, 111
- Warwick, R. S., Turner, M. J. L., Watson, M. G., & Willingale, R. 1985, Nature, 317, 218
- Yamauchi, S., Kawada, M., Koyama, K., Kunieda, H., & Tawara, Y. 1990, ApJ, 365, 532
- Yamauchi, S., & Koyama, K. 1993, ApJ, 404, 620
- Yamauchi, S., Ebisawa, K., Tanaka, Y., Koyama, K., Matsumoto, H., Yamasaki, N. Y., Takahashi, H., & Ezoe, Y. 2009, PASJ, 61, 225